JOURNAL OF SOLID STATE CHEMISTRY 12, 148–155 (1975)

Oxide Engineering*†

JOHN B. GOODENOUGH

Lincoln Laboratory, Massachusetts Institute of Technology, Lexington, Massachusetts 02173

Received July 3, 1974

Materials engineering involves not only the choice of a material having optimal intrinsic properties, but also economic fabrication in a form that optimizes its extrinsic properties. The intrinsic properties depend upon the relationship between structure and outer-electron behavior; and a general perspective of our descriptions of outer electrons in oxides is presented. Oxide engineering is illustrated by a consideration of heat mirrors for flat-plate solar collectors.

I. Heat Mirrors

This introductory paper has two objectives: (1) illustration of the process of materials engineering via a specific example, and (2) an overview of our descriptions of the outer electrons responsible for the magnetic, electric, optical, and elastic properties of oxides,

Materials engineering involves optimizing device performance through the choice and design of materials. As indicated in Fig. 1, the process begins with identification of a device. Its performance is characterized by engineering parameters, which may be defined as "figures of merit." The variables available to the metallurgist or ceramist, on the other hand, are chemistry, crystalline structure, and the physical state (sample shape, crystallinity, single or multiple phase, ...). The chemical composition and crystal structure determine the intrinsic properties; the physical state determines the extrinsic properties. The intrinsic properties are specified in terms of the phenomenological parameters of physical measurement; and materials-engineering analysis begins with a phenomenological model of the physical processes responsible for the intrinsic and extrinsic properties relevant to device performance. However, selection of the optimal material requires an understanding of the relationships between intrinsic properties and the composition and structure of the material.

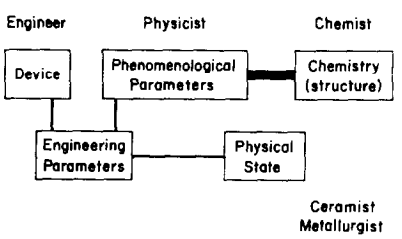

FIG. 1. Interactions involved in materials engineering.

Design of a solar flat-plate collector provides an illustration of materials engineering. An inexpensive solar-energy collector capable of efficiently delivering high-temperature heat would make conversion of solar energy to electricity an economically viable option. Mirror or lens concentrators are too expensive to construct and maintain; so there is need to design, if possible, an acceptable flat-plate collector.

A flat-plate collector consists of an absorber that converts the sun's radiant energy to heat. Because a hot absorber reradiates energy at ir frequencies (see Fig. 2), traditional strategy has been to tailor the absorber to

* This work was sponsored by the Department of the Air Force.

† Invited Paper, Keynote address.

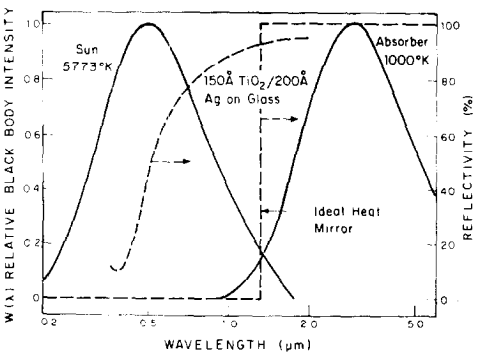

FIG. 2. Normalized black-body energy distributions (left ordinate) at temperatures of 5773 K (solar distribution) and 1000 K. Reflectivity (right ordinate) of an ideal heat mirror and a 150 Å TiO_2/200 Å Ag film.

have a high absorptivity α in the visible and low emissivity ε in the ir. Even if the absorber is covered by a glass plate that is isolated from it by a vacuum, ratios $\alpha/\varepsilon > 100$ are needed for efficient delivery of high-temperature heat. An alternate strategy is, in addition, to coat the inside of the glass cover plate with a film that transmits radiant energy in the visible spectrum, but reflects the ir energy from the absorber. The ideal reflectivity of such a "heat mirror" would be as shown in Fig. 2. Addition of such a film can greatly reduce the required α/ε ratio of the absorber (*1*).

In order to compare various candidate materials for the heat mirror, it is useful to have a generalized figure of merit. The idealized flat-plate collector of Fig. 3 permits definition and evaluation of a figure of merit for the heat-mirror material in terms of its complex dielectric constant and its thickness t, i.e., in terms of an intrinsic and an extrinsic

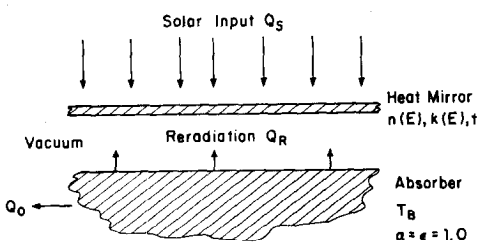

FIG. 3. Idealized flat-plate collector used to evaluate figures of merit for heat mirrors.

property. The model collector consists of a heat-mirror film, without the glass plate, that is isolated from a black-body absorber ($\alpha = \varepsilon = 1$) by a vacuum. Both film and absorber are infinite in two dimensions, and the sky temperature is taken to be 0 K. The figure of merit for such a collector is defined as the maximum collector efficiency at the optimum film thickness t for a given absorber temperature T_B:

$$F_A(T_B) \equiv Q_0/Q_s, \tag{1}$$

where the incident solar energy

$$Q_s = A \int_0^\infty W_s(E)\, dE \tag{2}$$

contains the normalization factor $A = 0.127 \times 10^{-4}$ for 0.08 W/cm^2 of solar energy on Earth. The thermal energy at temperature T_B delivered by the collector at thermal equilibrium is

$$Q_0 = A \int_0^\infty W_s(E)\,\mathrm{Tr}\,(E,t)\, dE - \int_0^\infty (1 - R(E,t))\, W_B(E)\, dE, \tag{3}$$

where the energy distribution function for black-body radiation

$$W_{S,B} = (8\pi/c^3 h^3)\, E^3/(\exp(E/kT_{S,B}) - 1) \tag{4}$$

is shown in Fig. 2 as the bell-shaped curves for $T_S = 5800$ K and $T_B = 1000$ K. Exact expressions (*2*) relate the reflectivity $R(E,t)$ and the transmission $\mathrm{Tr}(E,t)$ of the heat-mirror film to its optical constants $n(E)$ and $k(E)$, which are defined by the complex dielectric constant

$$\kappa(E) \equiv (n^2 - k^2) + i2nk. \tag{5}$$

The reflectivity of an ideal Drude conductor approaches that shown in Fig. 2 for the ideal heat mirror. The dielectric constant for the Drude conductor is calculated to be

$$\kappa(E) = 1 - (E_p^2/(E^2 + iE_c E)), \tag{6}$$

where, in c.g.s. units, the plasma and relaxation energies are

$$E_p = \hbar(4\pi Ne^2/m^*)^{1/2} \quad \text{and}$$
$$E_c \equiv \hbar/\tau_c = \hbar e/\mu_{op} m^*. \tag{7}$$

The plasma-cutoff energy can be varied as desired through control of the charge-carrier concentration N, and the sharpness of the cutoff, or the ir reflectivity, depends critically on having a high optical mobility $\mu_{op} = e\tau_c/m^*$.

Figure 4 shows F_A vs T_B for various ideal Drude mirrors. At each T_B a different film thickness t, also indicated in Fig. 4, is required to obtain F_A. An $E_c = 0.01$ eV is chosen as realistic. It corresponds to a $\mu_{op} \approx 100$ cm^2/V sec for $m^* = m_e$, the rest mass of the electron. It is immediately apparent that, even with ideal Drude mirrors ($E_c = 0.0$), interesting efficiencies at $T_B \approx 800$ K are only to be found if the black-body absorber is replaced by a selective surface having $\alpha \approx 1$, $\alpha/\varepsilon \gg 1$. The dashed line in Fig. 4 corresponds to $E_c = 0.01$, $\alpha = 1$, and $\alpha/\varepsilon = 5$. With this combination and a Carnot efficiency $(T_B - 373)/T_B$ for the heat engine, a maximum efficiency for conversion of solar energy to electrical energy would be 34% at $T_B = 800$ K. This compares favorably with the maximum efficiency to be anticipated from a photovoltaic cell.

Evaluation of real materials requires measurement of $\kappa(E)$, and figures of merit for several representative materials are presented elsewhere (*1*).

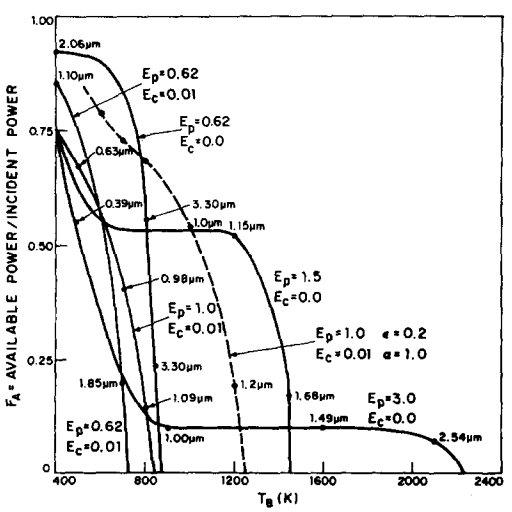

FIG. 4. Collector efficiency F_A vs absorber temperature T_B for different Drude mirrors and black-body absorbers. The optimum thickness t_{op} is also indicated for various points on the curves. Dashed curve is for an absorber having $\alpha/\varepsilon = 5$.

This exercise shows how an engineering parameter, such as $F_A(T_B)$, can be expressed in terms of intrinsic phenomenological parameters $\kappa(E)$, α, and α/ε and an extrinsic physical-state variable t. However, selection of the mirror material with optimum $\kappa(E)$ requires more fundamental knowledge. For this purpose, it is useful to have a perspective of the energy bands in solids.

II. Descriptions of Outer Electrons

In any description of outer electrons in solids, four energies are important: (1) the bandwidth w_b of one-electron states corresponding to like atomic orbitals in a periodic array, (2) the intraatomic-correlation splitting U or U', (3) the splitting energy V_q due to atomic displacements described by the wave vector $\mathbf{q}$, and (4) the energies $E_{n,l}$ of different atomic orbitals, which determine the relative positions of the energy bands.

To the lowest order in tight-binding theory,

$$w_b \approx 2zb, \tag{8}$$

where z is the number of like nearest neighbors and b is the nearest-neighbor transfer energy

$$b_{ij} \equiv (\psi_i, \mathscr{H}\psi_j) \sim \varepsilon_{ij}(\psi_i, \psi_j), \tag{9}$$

$\mathscr{H}$ is the perturbation of the electronic potential at $\mathbf{R}_j$ as a result of the presence of a like atom at $\mathbf{R}_i$. In oxides, the unperturbed cation wavefunctions

$$\psi_m = N_m(f_m - \sum_n \lambda_n \phi_n) \tag{10}$$

include covalent admixture of symmetrized anion functions ϕ_n to the same-symmetry free-cation function f_m. The parameter b varies with the overlap integral (ψ_i, ψ_j), increasing with decreasing metal–metal separation for direct interactions and with increasing covalent-mixing parameter λ_n for indirect interactions.

At a free atom, the energy U is the electrostatic interaction energy between two electrons in the same atomic orbital, and U' is that between two electrons in different orbitals of the same atomic manifold. These energies decrease

sensitively with increasing radial extension of the wave function and hence, in a solid, with increasing λ_n and b. In a solid, interatomic electron–electron interactions are also present. However, these are small relative to the intra-atomic interactions, so they can be incorporated into an effective intraatomic U.

Conventional band theory, in which $U = 0$, is applicable where $w_b \gg U$. This condition is generally fulfilled for outer s and p electrons, which are relatively loosely bound to the atomic nuclei and are active in chemical bonding.

Crystal-field theory is applicable in the opposite limit $w_b \ll U$. This condition is fulfilled for the tightly bound $4f$ electrons, which have a free-atom $U \approx 20$ eV and a $w_b \lesssim 0.1$ eV. Atoms having partially filled $4f$ shells carry a localized spin; and a spin-dependent transfer energy, which replaces b_{ij} of Eq. (9), introduces interatomic magnetic interactions. Charge transfer that requires an energy gives magnetic interactions described by superexchange perturbation theory (*3*). Because only virtual charge transfer occurs, the compound is an insulator. This condition is fulfilled if like atoms on equivalent lattice sites have an integral electron/atom ratio. Deviations from an integral number of electrons per like atom allow for real charge transfer; and the mobile charge carriers provide a ferromagnetic double-exchange contribution to the magnetic interactions (*4*), provided the time between electron transfers is short compared to the relaxation time of an atomic spin direction.

Lattice instabilities are induced by atomic displacements that split occupied states from unoccupied states by an energy V_q. In the crystal-field limit, the U responsible for localized atomic spins suppresses any instability that would decrease these spins, provided $V_q < U$. Cooperative Jahn–Teller distortions, with or without spin-orbit coupling, do not change the net atomic spin. Similarly, local lattice distortions that "dress" a mobile charge carrier, making it a small polaron, do not change the net atomic spin. For small polarons, $V_q \approx \varepsilon_A$ appears as an activation energy in the charge-carrier mobility.

At intermediate values of b, a $V_q \gtrsim U \approx w_b$ would induce a phase transition that tends

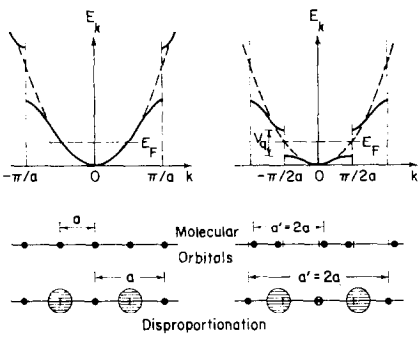

FIG. 5. Peierls instabilities for one-dimensional chains and half-filled bands: (a) metal–metal and (b) metal–anion–metal interactions.

to suppress the appearance of localized atomic moments. Consider, for example, Peierls instabilities, which are illustrated in Fig. 5 for one dimension and half-filled bands. A Peierls distortion produces a change in the translational periodicity that splits occupied states from unoccupied states; it may thereby induce a metal-to-semiconductor transition. Since the number of states stabilized by such a distortion increases with the magnitude of the induced gap V_q, the total stabilization varies as $V_q^2 \sim \delta^2$, where δ is the atomic displacement. Since the elastic restoring energy also varies as δ^2, spontaneous distortions only occur for a $w_b \lesssim V_q$. We define b_t as the critical value of b below which distortions occur. However, if $U > V_q$ at any b, lattice instabilities of this type are suppressed. At very small b, where U approaches the free-atom value, the electron-lattice interactions are smaller, and $V_q < U$. Therefore, we define b_t' as the critical value of b below which electron correlations suppress Peierls lattice instabilities. If $b_t' > b_t$, as is anticipated in simple oxides wherever the free-atom U is relatively large ($\gtrsim 10$ eV), Peierls instabilities are suppressed for all b, as illustrated in Fig. 6(a). However, if $b_t' < b_t$, then spontaneous crystallographic distortions may be encountered in the interval $b_t' < b < b_t$, as illustrated in Fig. 6(b).

Where the metal–metal interactions are direct, atomic displacements in a Peierls distortion may produce molecular-cluster metal–metal orbitals (which would include strong covalent mixing with any bridging

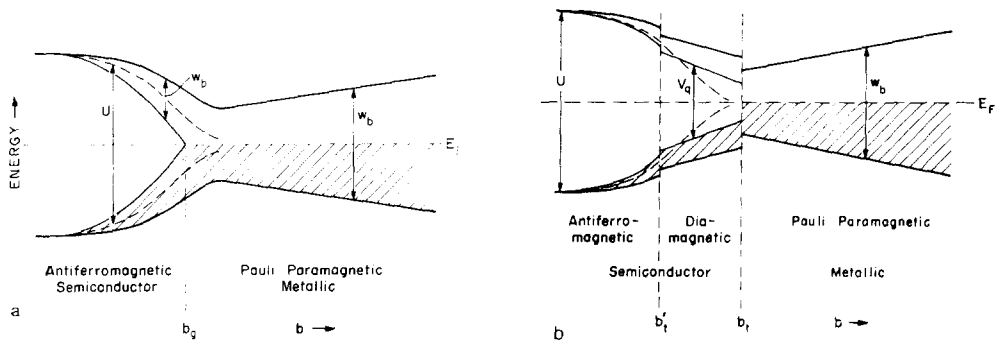

FIG. 6. Relative energy-level variations with bandwidth for a simple cubic array, $n_l = 1$, $T = 0$K, and (a) $b_t' > b_t$, (b) $b_t' < b_t$.

anions). This is the origin of the (8-N) rule of atomic bonding by s and p electrons. In the case of the half-filled band pictured in Fig. 5, pairing of the atoms along a linear chain produces singlet molecular-cluster states. This type of pairing is found in low-temperature VO_2. Spin pairing of the $V^{4+}:d^1$ electrons within a cluster (*5*) occurs at the expense of the U_{cl} for the molecular orbitals. U_{cl} is small because of the large extension of the molecular orbital.

Where the metal–metal interactions are indirect, via an intermediary anion, two types of Peierls distortion may be encountered: (1) the formation of metal–anion–metal clusters that expel the antibonding-electron density into the intercluster space, as in the arsenopyrites (*6*), and (*2*) interatomic disproportionation $M^{n+} + M^{n+} \rightarrow M^{(n+1)+} + M^{(n-1)+}$, as illustrated in Fig. 5. The compound $Tl^+Tl^{3+}F_4$ illustrates interatomic disproportionation of the type envisaged in Fig. 5, the diamagnetic cations having the configurations $Tl^+:6s^2$ and $Tl^{3+}:6s^0$. Spin pairing at the Tl^+ ion costs an energy U that is small relative to the energy gained by $Tl^{3+}:6s$–$O^{2-}:2p$ covalent mixing.

Transitions from a high-spin to a low-spin cation state represent intraatomic disproportionation. They occur at the expense of a $J^{intra} \sim (U-U')$ and are induced by a V_q that raises cation d orbitals with stronger covalent-mixing parameters λ_π relative to those with smaller λ_π; see Eq. (10) (*7*). In cubic symmetry, $V_q \doteq \Delta_c$ is the crystal-field splitting that separates the orbitally fivefold-degenerate d manifold into a threefold-degenerate t_2 and a twofold-degenerate e manifold. If $\Delta_c < J^{intra}$, the energy U stabilizes the high-spin state; if $\Delta_c > J^{intra}$, it doesn't. Thus FeS contains high-spin $Fe^{2+}:t_2^4e^2$ and FeS_2 low-spin $Fe^{2+}:t_2^6e^0$. Comparison of NiO and PdO shows that the octahedral-site $Ni^{2+}:t_2^6e^2$ configuration has two unpaired spins, whereas the Pd^{2+} ion assumes square, coplanar coordination in which one 4d orbital is empty and all the 4d spins are paired. The larger radial extension of the 4d vs 3d electrons not only increases V_q through stronger covalent mixing; it also reduces U.

From these arguments it follows that a large V_q and/or a small free-atom U may cause crystallographic distortions that suppress spontaneous magnetism in the interval $b_t' < b < b_t$. Outer s and p electrons, which have a small free-atom U and are active in interatomic interactions (large V_q), never exhibit spontaneous magnetism, whereas partially filled 4f shells always do (except where orbital and spin contributions cancel one another). In oxides, the 3d electrons may be itinerant as in superconducting TiO, strongly correlated (localized) as in the antiferromagnetic insulator MnO, intermediate without crystal distortion ($b_t' > b_t$) as in the antiferromagnetic conductor $CaCrO_3$, or intermediate with magnetism suppressed ($b_t' < b < b_t$) as in low-temperature $LaCoO_3$ (low-spin $Co^{III}:t_2^6e^0$ without crystal distortion) and low-temperature VO_2 (singlet V^{4+}–V^{4+} pairs). Outer 4d and 5d electrons tend either to be itinerant or to induce crystallographic

structures that suppress spontaneous magnetism (*8*).

Where Fig. 6(a) applies ($b_t' > b_t$), the T–b phase diagram is as shown schematically in Fig. 7. The maximum in the Néel temperature T_N occurs at, or near, the value of $b = b_c$ beyond which the superexchange perturbation expansion fails to converge. For $b < b_c$, intraatomic exchange dominates the interatomic interactions ($U \gg w_b$) and

$$kT_N \sim z|J|S(S+1) \sim w_b^2/zU, \qquad (11)$$

where the Heisenberg exchange parameter J for half-filled orbitals ($n_l = 1$) follows from the second-order (electron transfer requires the energy U) perturbation

$$\Delta\varepsilon \approx -z(b^2/U)\sin^2(\theta/2) = \text{const} + z(2b^2/4S^2U)\mathbf{S}_i\cdot\mathbf{S}_j. \qquad (12)$$

The Pauli exclusion principle restricts electron transfer to antiparallel-spin electrons, so the spin-dependent transfer energy is $b\sin(\theta/2)$. (Rotation of spin vectors through an angle θ goes as the half-angle rather than as the angle.) Construction and discussion of this and similar diagrams for other values of n_l may be found elsewhere (*8*). A discussion, with applications, of the change with n_l from antiferromagnetic to ferromagnetic ordering and of the magnitude of the spin contribution to atomic moments as a function of b is also available (*9*).

Application of these concepts to oxides is illustrated by the cubic monoxides. Construction of the relevant s and p itinerant-electron bands is shown schematically in Fig. 8. E_M is the electrostatic Madelung energy and E_I is the energy gained by transferring an electron from an O^{2-} ion to an M^{2+} ion. The larger the energy E_M–E_I, the larger the energy gap E_g.

It is not possible to dope an oxide p-type by introducing holes into the O^{2-}:$2p$ bands. Optically excited holes and electrons generally undergo fast electron-hole recombination. However, they may be separated by a depletion layer bordering a solid–aqueous interface. In this case, the holes recombine with electrons from the OH^- ions in the liquid to evolve O_2 molecules:

$$2OH^- - 2e \rightarrow (1/2)O_2 + H_2O. \qquad (13)$$

This latter reaction provides the possibility of photoelectrolysis and is therefore of interest for the direct conversion of solar energy to chemical energy. In peroxides, holes in the O^{2-}:$2p$ bands combine in molecular-cluster orbitals to form the complex anions $(O_2)^{2-}$.

Introduction of electrons into the s conduction band is only possible for the heavier cations. Oxides containing itinerant charge carriers in a $5s$ or $6s$ conduction band include Tl_2O_{3-x}, SnO_2:Sb and In_2O_3:Sn. Conductors transparent in the visible are of interest for a variety of applications, including heat mirrors for solar-energy flat-plate collectors; and n-type SnO_2 or In_2O_3 fit this description. Filled $5s^2$ or $6s^2$ cores may also be stable in oxides. As in PbO, spontaneous polarization of such a core may occur, atomic displacements stabilizing O^{2-}:$2p$ states (via stronger covalent mixing) at the expense of cation s–p hybridization.

Rare-earth oxides possess $5d$ bands that

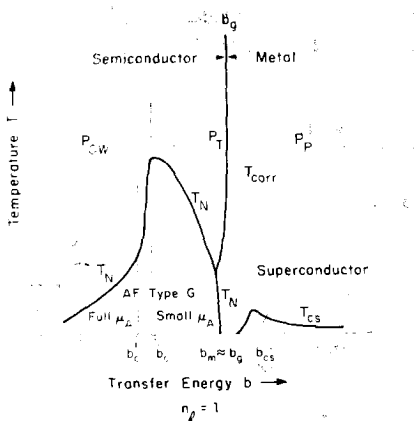

FIG. 7. Schematic T–b phase diagram for a simple cubic array with $n_l = 1$ and $b_t' > b_t$.

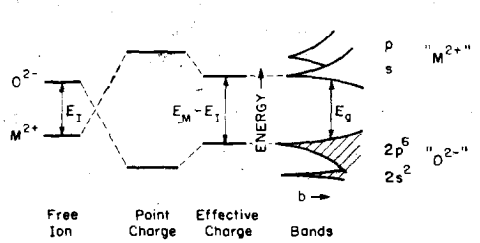

FIG. 8. Relevant s and p bands for cubic monoxides.

overlap and hybridize with the 6*s* band. They also possess strongly correlated (localized) $4f^n$ manifolds separated by a large U or U', where $U > U' > E_g$. If the energy of a $4f^{n+1}$ manifold lies above the edge E_c of the 5*d*–6*s* conduction band, it remains empty. If, in addition, the corresponding $4f^n$ manifold lies below the edge E_V of the 2*p* valence band, it remains full and only the $4f^n$ core state is stable in the oxide. Two core states may be stabilized if either the $4f^{n+1}$ or the $4f^n$ level falls in the gap E_g. If the $4f^n$ level corresponds to a free-ion valence state Ln^{3+}, then it follows that the $4f^n$ level falls in E_g if Ln = Ce, Pr, or Tb, and the $4f^{n+1}$ level falls in E_g if Ln = (Sm), Eu, Tm, or Yb. For the other lanthanides, neither manifold falls in E_g. In the system $Eu_{1-x}Gd_xO$, the Eu^{2+}:$4f^7$ level lies 1.1 eV below E_c. The Gd ion also carries a $4f^7$core, the extra electron per Gd entering the 5*d*–6*s* conduction band.

Similar reasoning holds for the d^n manifolds in transition-metal oxides. Therefore, the existence of multiple formal-valence states for transition-metal ions in oxides indicates that U or U' may be smaller than E_g. In the case of octahedral-site vanadium, for example, the existence of VO, V_2O_3, VO_2, and V_2O_5 would seem to require placing the d^3, d^2, and d^1 manifolds within $E_g \approx 6$–7 eV. Therefore, a $U' \lesssim 3$ eV is anticipated, which introduces the condition $w_b \approx U$. It also appears that $V_q \approx U$ in VO_2 and V_2O_3, which gives rise to interesting crystallographic distortions that suppress, or diminish, the spin moment at the vanadium cations. In the spinels $M^{2+}[V_2^{3+}]O_4$, on the other hand, a $U > V_q$ suppresses crystallographic distortions, although disproportionation of $Ni[V_2]O_4$ makes this phase unstable to reduction of Ni^{2+} ions by oxidation of the V^{3+} ions (*10*).

Figure 9 shows a schematic energy diagram for ideally dense VO. (As prepared, VO contains vacancies and tetrahedral-site vanadium—probably V^{5+} ions—which complicates the diagram.) The 3*d* orbitals of *e* symmetry, which form the σ^* band, are raised in energy above E_F by covalent mixing with the O^{2-}:2*p* orbitals. Direct V–V interactions reduce $U = U_t$ for the t_2 orbitals and broaden the V^{2+}: $t_2^3e^0$ and V^+:$t_2^4e^0$ levels into t_2^3 and t_2^4 bands

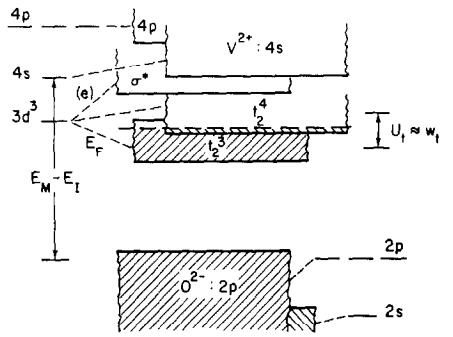

FIG. 9. Schematic energy diagram for ideally dense VO.

that just overlap ($U_t \approx w_t$). No spontaneous magnetism is observed despite considerable exchange enhancement of the magnetic susceptibility (*11*).

In contrast, an octahedral-site Cr^{3+}:$t_2^3e^0$ cation always carries, in oxides, a full localized spin $S = 3/2$, the larger effective nuclear charge contracting the radial extension of the t_2 orbitals sufficiently to make $U_t > w_t$. A similar contraction of the t_2 orbitals at an octahedral-site V^{3+}:$t_2^2e^0$ ion might be expected to guarantee a localized spin $S = 1$, as found in the spinels $M^{2+}[V_2^{3+}]O_4$. However, a $U_t' < U_t$ is the critical energy, and V_2O_3 is complicated by a $V_q \approx U_t' \approx w_t$ (*12*).

In MnO, a $\Delta_c < J^{intra}$ results in a high-spin Mn^{2+}:$t_2^3e^2$ manifold with energy near the center of E_g. The half-filled 3*d* orbitals give a localized Mn^{2+}-ion spin $S = 5/2$, in accordance with Hund's rule, and antiferromagnetic interactions dominated by 180° Mn^{2+}–O^{2-}–Mn^{2+} superexchange. As illustrated in Fig. 10,

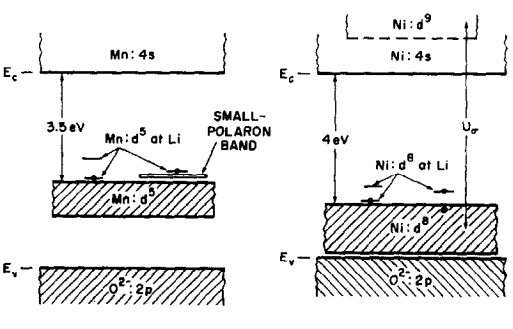

FIG. 10. Schematic energy diagrams for Li-doped MnO and NiO.

Li-doped MnO contains mobile, small-polaron holes having an $\varepsilon_A \approx 0.3$ eV (*13*).

In NiO, stronger covalent mixing between O^{2-}:2*p* and Ni:*e* orbitals raises the magnetic-ordering temperature T_N and sufficiently broadens the bandwidth of the Ni^{2+}:$t_2^6e^2$ configuration to suppress small-polaron formation, except if the holes are trapped at Li^+-ion centers.[13] The fact that the critical value $b = b_c'$ for small-polaron formation is less than b_g (see Fig. 6(a)) is consistent with a $b_t' > b_t$ in simple Ni^{2+} compounds like NiO and NiS. In $K_2Ni(CN)_4$, on the other hand, the complex cyanide ion reduces *U*, via covalent mixing with carbon, and simultaneously reduces w_b. Square-coplanar bonding (*14*) suppresses the magnetic moment, indicating $b_t' < b < b_t$ and hence a $V_q > U, w_b$.

Note added in proof. Jeitschko and Donohue (*Acta Cryst.*, in press), point out inconsistencies in published data to argue that the arsenopyrites illustrate metal–metal bonding.

Acknowledgments

I would like to thank J. C. C. Fang and T. B. Reed for permission to use Figs. 2–4, which were taken from Ref. (*1*).

References

1. J. C. C. Fan, T. B. Reed, and J. B. Goodenough, *Proceedings 9th Intersociety Energy Conversion Conference, San Francisco, Aug. 1974*, p. 341. Soc. of Automotive Engineers, Inc., N.Y.
2. O. S. Heavens, "Optical Properties of Thin Solid Films," p. 69. Dover Publications Co. (1965).
3. P. W. Anderson, *Phys. Rev.* **115**, 2 (1959).
4. C. Zener, *Phys. Rev.* **82**, 403 (1951); P. W. Anderson and H. Hasegawa, *Phys. Rev.* **100**, 675 (1955); P-G. De Gennes, *Phys. Rev.* **118**, 141 (1960).
5. J. B. Goodenough, *Phys. Rev.* **117**, 1442 (1960).
6. J. B. Goodenough, *J. Solid State Chem.* **5**, 144 (1972).
7. J. B. Goodenough, *Bull. Soc. Chim. France*, p. 1200 (1965).
8. J. B. Goodenough, *Prog. Solid State Chem.* **5**, 145 (1972); "New Developments in Semiconductors" (P. R. Wallace, R. Harris, and M. J. Zuckerman, Eds.), p. 105, Nordhoff International Leyden, 1973.
9. J. B. Goodenough, *J. Solid State Chem.* **7**, 428 (1973).
10. D. B. Rogers, R. J. Arnott, A. Wold, and J. B. Goodenough, *J. Phys. Chem. Solids* **24**, 347 (1963).
11. M. D. Banus and T. B. Reed, "The Chemistry of Extended Defects in Non-metallic Solids." (L. Eyring and M. O'Keeffe, Eds.), p. 488. North Holland, Amsterdam, 1970.
12. J. B. Goodenough, *Progr. Solid State Chem.* **5**, 145 (1972).
13. A. J. Bosman and H. J. Van Daal, *Adv. in Phys.* **19**, 1 (1970).
14. L. Pauling, "The Nature of the Chemical Bond." Third ed., p. 168 Cornell Univ. Press, Ithaca, N.Y., 1960.